Simultaneously Improved Bendability and Strength of Al–Mg–Si–Cu–Zn Alloys by Controlling the Formation and Evolution of Primary Fe-Rich Phase

Du, Jinqing; Li, Gaojie; Guo, Mingxing; Lu, Wenyi; Dong, Qijuan; Zhuang, Linzhong

DOI
10.1002/adem.202300376

Publication date
2023

Document Version
Final published version

Published in
Advanced Engineering Materials

Citation (APA)
Du, J., Li, G., Guo, M., Lu, W., Dong, Q., & Zhuang, L. (2023). Simultaneously Improved Bendability and Strength of Al–Mg–Si–Cu–Zn Alloys by Controlling the Formation and Evolution of Primary Fe-Rich Phase. *Advanced Engineering Materials*, *25*(17), Article 2300376. https://doi.org/10.1002/adem.202300376

ADVANCED ENGINEERING MATERIALS
www.aem-journal.com

Simultaneously Improved Bendability and Strength of Al–Mg–Si–Cu–Zn Alloys by Controlling the Formation and Evolution of Primary Fe-Rich Phase

Jinqing Du, Gaojie Li, Mingxing Guo, Wenyi Lu, Qijuan Dong, and Linzhong Zhuang*

In present work, the formation, evolution, and distribution of the primary Fe-rich phase in an Al–Mg–Si–Cu–Zn–Fe–Mn alloy are coupling controlled by ultrasonic melt treatment (USMT) and thermomechanical processing (TMP). It is shown in the results that the size of grains and Fe-rich phase in the as-cast state can be greatly reduced by the applied optimum USMT at 680 °C. Additionally, the transformation rate of β-Fe-rich phase to α-Fe-rich phase can be also enhanced. After the coupling control of USMT and TMP, the number density and distribution uniformity of multiscale Fe-rich particles can be greatly increased or improved, which contributes to the fine-grained recrystallization microstructure and weakened texture. Finally, compared with the 6xxx series Al alloys (such as AA6016 and AA6111), the alloy sheet in the pre-aging state exhibits substantially improved bendability and strength (the plastic strain ratio and tensile strength are 0.67 and 304 MPa, respectively). The effect of USMT on the formation and transformation of primary Fe-rich phase and the mechanisms of improved bendability and strength are deeply discussed.

1. Introduction

As one of the most promising materials for lightweight automobiles, Al–Mg–Si–Cu alloys have been widely used in automotive fields due to their desirable properties such as high strength-to-weight ratio and good formability, high corrosion resistance, and recycling potential. However, the current bake-hardening response (BHR) during the short paint bake-hardening cycle of commercial Al–Mg–Si alloys (e.g., AA6016) is limited to 80–100 MPa.[1,2] To improve the BHR of Al–Mg–Si–Cu alloys, a lot of researches have been carried out from the aspects of adjusting Mg/Si ratio, and microalloying (such as trace Ag and Li) and optimizing heat-treatment process (TMP).[3–6] Unfortunately, all these strategies merely achieved some limited contribution. Recently, it was found that Zn addition in Al–Mg–Si–Cu alloys can drastically improve the BHR (about 135MPa), which was ascribed to enhanced formation of clusters, Guinier–Preston zones, and β" precipitates, as well as higher number density of fine β" precipitates.[7,8] Nevertheless, it is reported that high Zn content in Al–Mg–Si–Cu alloys could lead to the coarsening of recrystallization microstructure, decrease of plastic strain ratio, and increase of planar anisotropy, that is, deterioration of formability.[9,10] Therefore, improving the formability of high-BHR Al–Mg–Si–Cu–Zn alloys is inevitable.

Nowadays, several researches have shown that the regulation of Fe-rich particles in heat-treatable aluminum alloys (e.g., 6xxx and 7xxx alloys) by appropriate TMPs can not only refine recrystallization grains, weaken texture, and improve formability, but also expand the utilization potential of recycled aluminum.[11,12] However, the Fe-rich phase in Al–Mg–Si alloys is generally brittle and hard, and heavily segregated along grain boundaries. Despite the fact that most of the Fe-rich phase can be broken into small particles during TMP, microcracks and microvoids would be induced by coarser Fe-rich particles that are not completely broken, further deteriorating the bendability which is very important for the connection of interior and exterior panels of automobile.[13] Additionally, the nonuniform distribution of Fe-rich particles also results in poor mechanical properties.[14,15] Hence, it is significant to regulate the size and distribution of Fe-rich phase, and further effectively govern the Fe-rich particles, microstructure and texture, making the novel Al–Mg–Si–Cu–Zn alloys sheet exhibit excellent formability/bendability.

The type of Fe-rich phases in Al–Mg–Si alloys, such as, β-Al_5FeSi, α-Al_8Fe_2Si (possibly α-$Al_{12}Fe_3Si_2$), α-$Al_{15}(FeMn)_3Si_2$, and $Al_{13}Fe_4$, varies with different alloy compositions, cooling rates, and external fields during solidification. For example, when

J. Du, M. Guo, L. Zhuang
State Key Laboratory for Advanced Metals and Materials
University of Science and Technology Beijing
Beijing 100083, China
E-mail: mingxingguo@skl.ustb.edu.cn

G. Li
Department of Materials Science and Engineering
Delft University of Technology
2628 CD Delft, The Netherlands

M. Guo, L. Zhuang
Beijing Laboratory of Metallic Materials and Processing for Modern Transportation
University of Science and Technology Beijing
Beijing 10083, China

W. Lu, Q. Dong
Shandong Key Laboratory of Advanced Aluminium Materials and Technology
Weiqiao-UCAS Science and Technology Park
Binzhou, Shandong Province P.C.256606, China

The ORCID identification number(s) for the author(s) of this article can be found under https://doi.org/10.1002/adem.202300376.

DOI: 10.1002/adem.202300376

Mn is contained, β-$Al_5(FeMn)Si$ can be formed due to the replace of Mn for Fe.[11,16–19] To improve the morphology, size, and distribution of Fe-rich phases, various methods have been used: 1) adding trace elements or grain refiner;[17,20] 2) applying ultrasonic or electromagnetic fields to refine the microstructure during solidification;[21–24] 3) using thermomechanical processing (TMP), such as, homogenization can promote the transformation detrimental β-Al_5FeSi phase to the positive α-$Al_{15}(FeMn)_3Si_2$, and rolling or extrusion can broke the Fe-rich particles.[25–27]

Among them, ultrasonic melt treatment (USMT), accompanied with advantages of simple operation, low cost, and environmental protection, is a promising economical technology for improving the quality of cast ingots.[28–33] It is generally accepted that the mechanisms of USMT on solidification microstructure can be ascribed to two aspects: 1) the cavitation bubbles generated by acoustic cavitation causes local undercooling of the nearby melt, resulting in a large number of fine crystal nuclei around the cavitation bubble; simultaneously, the jets generated by collapse of cavitation bubbles, along with high pressure and high temperature, can continually attack and broke the dendritic structure; 2) acoustic streaming improves solute homogeneity which further homogenizes the spatial distribution of dendrites and intermetallic phases.[34,35] Extensive works have shown that USMT can refine grain size, improve microstructural homogenization, and enhance the properties of Al alloys.[36–39] In addition, it is suggested that USMT can inhibit the macrosegregation and boost the formation of fine and uniformly distributed Fe-rich phases in Al–Si–Fe alloys.[40,41] And, USMT can also change the shape of Fe-rich phases from coarse Chinese script to fine polygonal in Al–Si alloys.[23] However, the effect of USMT on the solidification microstructure (especially the changes of Fe-rich phases) and mechanical properties in the novel Al–Mg–Si–Cu–Zn alloys has not been reported yet.

Accordingly, in present work, the effect of USMT on the formation of Fe-rich phases in an Al–3Zn–0.9Mg–0.7Si–0.2Cu–0.4Fe–0.5Mn–0.1Ti (wt.%) alloy was comparatively studied, and the mechanical property of the alloy sheets were tested. Scanning electron microscope (SEM), electron backscatter diffraction (EBSD), and transmission electron microscope (TEM) were used to characterize the difference of microstructural evolution; further, the mechanical property and formability of the alloy sheets were detected by tensile test and bending test.

2. Experimental Section

2.1. Materials Preparation

In present work, the studied Al–3Zn–0.9Mg–0.7Si–0.5Mn–0.4Fe–0.2Cu–0.1Ti (wt.%) alloy was prepared by high purity Al (99.99%), pure Mg and Zn, Al–20wt%Si, Al–50wt%Cu, Al–20wt%Fe, Al–10wt%Mn, and Al–10wt%Ti master alloys. The smelting of the raw materials was carried out in a corundum crucible (with the dimensions of 40 mm bottom diameter, 70 mm top diameter, and 60 mm height, respectively) which was placed in an electric resistance furnace. After the melting of raw materials, the melt was held at 750 °C for 10 min for the homogenization of elements and then slowly cooled down to specific temperature, preparing for the implementation of USMT. The melt volume of the melt was about 140 cm^3.

2.2. USMT

The installation of ultrasonic consisted of an ultrasonic generator (1.5 kW), a magnetostrictive transducer (21 kHz), and an ultrasonic sonotrode (diameter: 20 mm). A K-type thermocouple was used to measure the temperature of melt. The schematic diagram of the USMT setup shown in **Figure 1** indicates the locations of sonotrode and thermocouple. Before treatment, the sonotrode was preheated to 450 °C above the melt to weaken the chilling effect. To understand the effect of temperature on USMT, the temperature for implementation of USMT was set as 720, 680, and 640 °C, respectively. During treatment, the sonotrode was immersed 20 mm below the melt surface and the handling time was 5 min. The melt temperature was held constant by controlling the power of the resistance furnace throughout the process. After that, the sonotrode and thermocouple were withdrawn from the melt and the crucible was extracted from the furnace. Immediately, the melt was directly poured into a water-cooling mold with a gauge of 20 mm (cross section) × 150 mm (height). Three ingots were obtained (referred as US-720, US-680, and US-640, respectively), corresponding to the three temperatures for implementation of USMT. For comparison, another ingot without USMT was prepared in the same way and was referred as non-US.

2.3. TMP

Generally, homogenization treatment was necessary but treated as a high-cost factor for deformable aluminum alloys, and it was in great urgent to design novel compact process by shortening or omitting the homogenization treatment.[42] The traditional TMP of Al–Mg–Si–Cu–Zn alloys included homogenization, hot-rolling, first cold-rolling, intermediate annealing, second cold–rolling, and solid solution. Among them, the temperature of homogenization treatment was up to 555 °C, and the preservation time was as long as 30 h or even longer, which led to expensive production costs. Accordingly, in present work, a

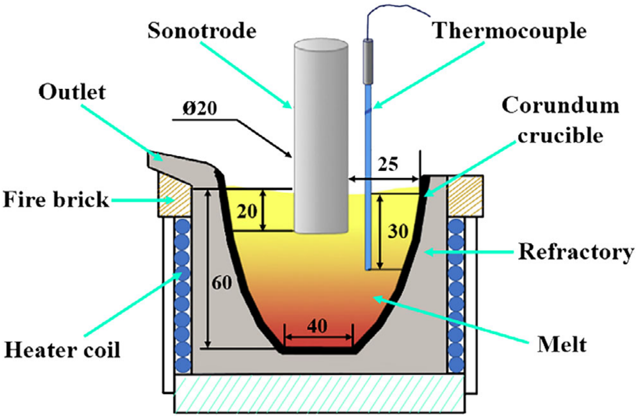

Figure 1. The schematic diagram of the ultrasonic melt treatment (USMT) setup.

low-cost short flow TMP was designed for the preparation of 1 mm sheets through reducing the homogenization time by 40% and omitting the intermediate annealing process. The specific processing was described as follows

The ingots were first hot-rolled from 20 to 6 mm after keeping at 500 °C for 1 h, and then the 6 mm hot-rolled sheets were homogenized in an air furnace by a treatment of 485 °C/3 h→555 °C/10 h→ cooled down to room temperature out of furnace. After that, the homogenized sheets were continuously cold-rolled to normative gauge of 1 mm at room temperature without intermediate annealing. The final 1 mm cold-rolled sheets were solution treated in a salt bath furnace at 555 °C for 2 min instantly followed by water quenching to room temperature. For the study of bendability and tensile properties, the quenched alloy sheet was immediately pre-aged with evenly variable temperatures from 80 to 40 °C in 12 h.

2.4. Characterization of Microstructure

Phenom XL SEM equipped with energy spectrometry (EDS) was used to characterize the morphology, size, distribution, and chemical composition of Fe-rich phases in the different conditions. To ensure the accuracy of statistics, 20 SEM microstructure images of each specimen were acquired, and 10 EDS analysis spots were selected to confirm the chemical composition of each phase. The SEM specimens were mechanically ground using abrasive paper and then polished according to standard procedures. Additionally, Image-Pro software was used to quantitatively analyze the size and number density of Fe-rich phase particles.

The grain size, orientation, and texture of solution treated sheets were measured by EBSD with operating voltage of 20 kV, working distance of 15–20 mm, and a scanning step size of 2 μm. The EBSD specimens were prepared by electrolytic polishing in a solution comprising 5% vol perchloric acid and 95% vol ethanol with a voltage of 20 V for 7s at −20–−30 °C after mechanical grinding.

Tecnai G2F20 S-Twin field-emission TEM equipped with an EDS probe was used to characterize the dispersoids existing in the solution treated sheets. The TEM foils were prepared by mechanically grinding to the thickness of about 100 μm, and then twin-jet electropolished using an electrolyte containing 75 vol% methanol and 25 vol% nitric acid at −20–−30 °C. The operating voltage of device was 20 kV and the crystal zone axis was $[001]_{\mathrm{Al}}$.

2.5. Property Testing

The mechanical properties of the pre-aged alloy sheets, including yield strength (YS), ultimate tensile strength, elongation, strain-hardening exponent (n), and plastic strain ratio (r), were tested at room temperature using an MTS 810 electrohydraulic servo universal performance machine. The tensile specimens were cut from 1 mm cold-rolled sheets along the rolling direction according to GB/T 5028. The *n* value represents the ability of metal materials to resist uniform plastic deformation, and it was calculated over the 5%–15% strain range according to ISO 10275 method. The *r* value reflects the ability of metal sheets to resist thinning or thickening when subjected to tension in a plane, and it was calculated as tensile strain reaching 15% according to ISO 10113 method.

In present work, the Semi-Guided Bend Test was adopted according to the American standard (ASTM 290) to test the bendability of the pre-aged alloy sheets. The experimental device is same as that reported in ref. [43]. The bending die was 80 mm in height, 40 mm in width, and 2 mm or 1 mm in thickness, that is, the bending radius of the pressure head (R) was 1 or 0.5 mm. The bending specimen was a rectangle of 70 mm (rolling direction) × 20 mm (transverse) cut from 1 mm cold-rolled sheets.

3. Results

3.1. Evolution of Fe-Rich Phase

Figure 2 shows the as-cast microstructure of the four experimental ingots. As shown in Figure 2a–d, the Fe-rich phase (the white particles) in non-US seriously segregates along grain boundaries in the form of coarse reticulations, and that in US-720 presents mixed large-size reticulations and strips with smaller thickness (which is defined as the width of Fe-rich phase occupied at grain boundaries). In contrast, the fine short-rodlike Fe-rich phase in US-680 has the minimum thickness (almost all <0.5 μm) and best distribution uniformity. However, the Fe-rich phase in US-640 has a similar morphology and distribution with that in non-US. In contrast, the average grain sizes of the four alloys are 30, 24, 15, and 28 μm, respectively. Obviously, implementation of USMT at 680 °C can significantly refine the as-cast grains, reduce the thickness of Fe-rich phase, and improve its distribution uniformity. But the USMTs at 720 and 640 °C only have a weak effect on the as-cast microstructure, the former may be ascribed to the high temperature of the melt and the latter may be due to the fact that the melt has nearly solidified. Accordingly, the optimum temperature for implementation of USMT is 680 °C, and following studies will only focus on samples non-US and US-680.

Figure 2e,f shows the chemical composition of Fe-rich phase in the two samples. It can be seen that the composition elements and proportion of each element in the Fe-rich phase of the two samples are basically same, indicating that are the same phase, β-$\mathrm{Al_5(FeMn)Si}$ phase (hereafter, referred to β-Fe-rich phase). In other words, USMT does not change the type of Fe-rich phase. However, the content of Fe, Mn, and Si in the β-Fe-rich phase of US-680 is less than that of non-US, which should be related to a higher diffusion rate of solute elements and will be analyzed in Discussion section.

Figure 3 shows the microstructure of non-US and US-680 after homogenization. It can be found that fine spherical particles are formed in both the samples, which means that the transformation of β-$\mathrm{Al_5FeSi}$ phase to α-$\mathrm{Al_{15}(FeMn)_3Si_2}$ phase (hereafter, referred to α-Fe-rich phase) has occurred. As shown in Figure 3a, only a few slender branches of β-Fe-rich phase have been spheroidized in non-US. However, almost all of β-Fe-rich phase has been transformed into spherical α-Fe-rich phase in US-680 as shown in Figure 3b.

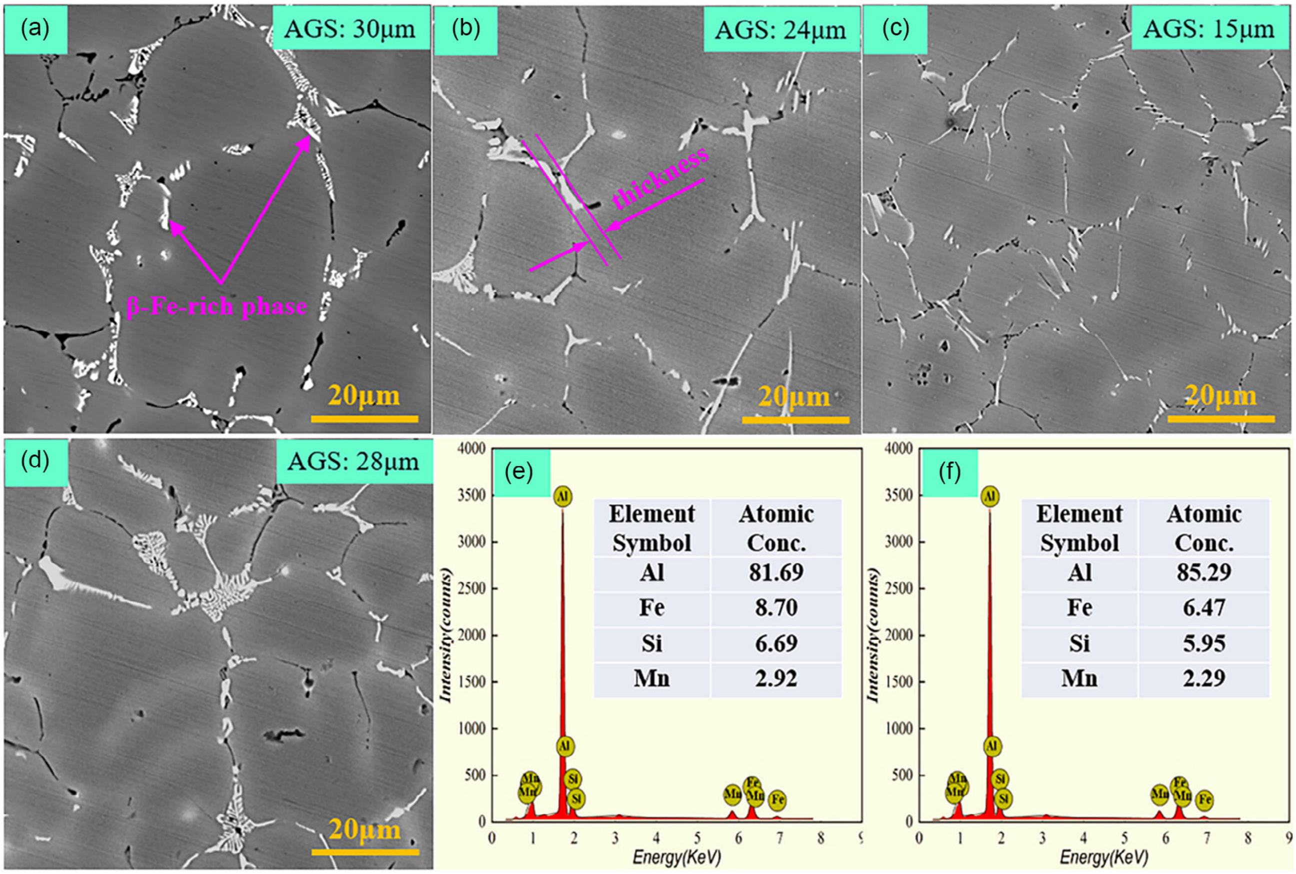

Figure 2. As-cast microstructure of the four experimental ingots. a) non-US; b) US-720; c) US-680; d) US-640; and e,f) the chemical composition of Fe-rich phase in the non-US and US-680, respectively.

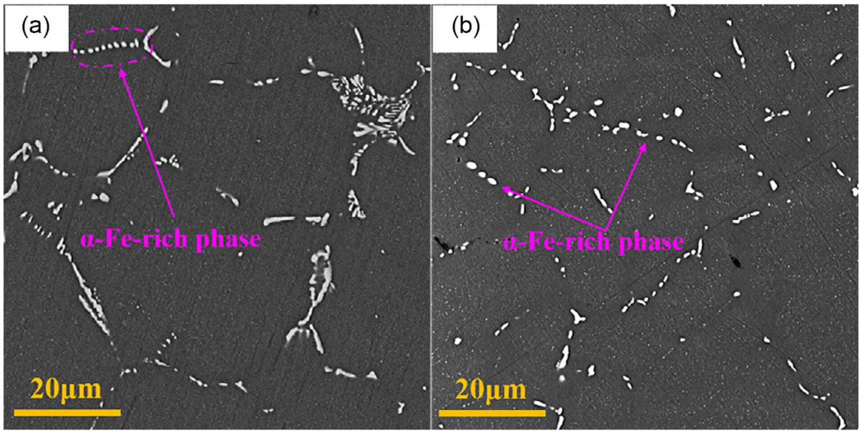

Figure 3. Microstructure of non-US sample and US-680 after homogenization: a) non-US; b) US-680.

Table 1 lists the number density and chemical composition of α-Fe-rich phase in the two samples. Obviously, the number density of α-Fe-rich phase in US-680 is much more (about four times) than that of non-US, which indicates that USMT significantly promotes the transformation of β-Fe-rich phase to α-Fe-rich phase. Comparing the chemical composition of the two phases, it can be found that the content of Fe and Si in α-Fe-rich phase is less than that in β-Fe-rich phase, while the content of Mn is higher. It means that the transformation of $\beta \rightarrow \alpha$ concerns diffusion of Fe and Si, and absorption of Mn.

Cold-rolling does not contribute to transformation but only refinement of Fe-rich phase due to the low processing temperature. In the process of solid solution, though the temperature is appropriate, the handling time is too short for transformation of

Table 1. Number density and chemical composition of α-Fe-rich phase in homogenized non-US and US-680.

Sample	Number density	Chemical composition [at%]			
	$\times 10^9$ m^{-2}	Al	Fe	Si	Mn
Non-US	4.22 ± 0.23	83.03	8.28	5.36	3.33
US-680	16.41 ± 0.37	85.69	6.15	4.60	3.56

Fe-rich phase. Hence, the TMPs after homogenization only change the size and distribution of Fe-rich particles but have no effect on the chemical composition. **Figure** 4a,b shows the microstructure of non-US and US-680 in solid solution condition. It can be intuitively observed that the Fe-rich particles in US-680 have smaller size and more uniform distribution state. Figure 4c,d shows the relationship between the size of Fe-rich particles and its relative frequency. Apparently, the Fe-rich particles in non-US have a wider size distribution range with a maximum size of 17.4 μm, while that in US-680 mainly range from 0–4 μm, and the maximum size is only 9.6 μm. It has been revealed that both the coarse (>1 μm) and fine (<1 μm) particles have important effect on the recrystallization microstructure and texture, that is, the coarse particles facilitate the occurrence of particle stimulated nucleation (PSN), while fine particles retard recrystallization grain growth (pinning effect).[44] Therefore, it is necessary to quantitatively calculate the number density, average size, and volume fraction of both coarse and fine Fe-rich particles, and the results are listed in **Table 2**. The number density of the coarse and fine Fe-rich particles in US-680 reach to 15.1×10^9 and 7.3×10^9 m^{-2}, respectively, which is much higher than that of non-US. Simultaneously, they both have smaller average size and higher volume fraction.

3.2. Bendability and Mechanical Properties

As stated in Section 2.5, the bendability of non-US and US-680 pre-aged sheets was tested by Semi-Guided Bend Test. After bending, the convex surface is examined for evidence of cracks or surface irregularities. When complete fracture does not occur,

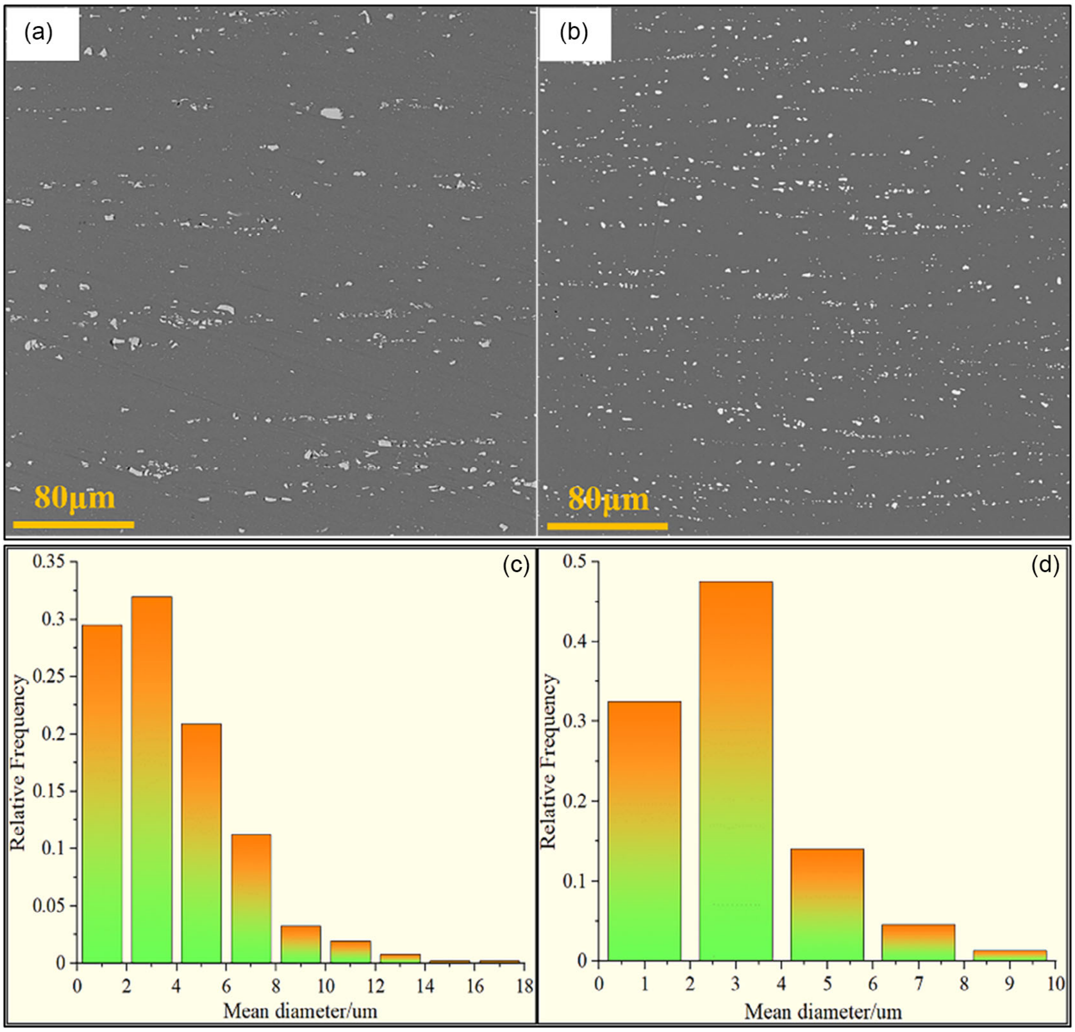

Figure 4. a,b) Microstructure of solution treated sheets non-US and US-680, respectively; c,d) size distribution of Fe-rich particles in non-US and US-680, respectively.

Table 2. The number density, average size, and volume fraction of Fe-rich phase particles in solution treated sheets non-US and US-680.

Alloy	Fe-rich particles					
	Coarse (>1 μm)			Fine (<1 μm)		
	Number density [10^9 m^{-2}]	Average size [μm]	Volume fraction [%]	Number density [10^9 m^{-2}]	Average size [μm]	Volume fraction
Non-US	8.8 ± 0.4	3.92 ± 0.12	10.7 ± 0.4	3.6 ± 0.3	0.67 ± 0.09	3.2 ± 0.4
US-680	15.1 ± 0.2	2.76 ± 0.16	15.5 ± 0.3	7.3 ± 0.5	0.52 ± 0.13	6.5 ± 0.1

the criterion for failure is the number and size of cracks or surface irregularities, according to the standard ASTM E290. The bending performance is usually defined as R/t, where R is the bending radius of the pressure head, and t is the thickness of the bending specimen. Under the same condition, smaller R/t and less surface irregularities mean better bendability. **Figure 5**a–d shows the results of bending test. Obviously, when $R/t = 1$, distinct uneven folds exist on the convex surface of non-US, while the surface of US-680 is quite smooth without any surface irregularity; when $R/t = 0.5$, noticeable macrocracks are formed on the convex surface of non-US, but only extremely pointy undulations occur on the convex surface of US-680. Without any doubt, the US-680 has a substantially improved bendability.

Figure 5e shows the tensile engineering stress–strain curves of non-US and US-680 pre-aged sheets, and corresponding mechanical property parameters are presented in the insert image. It can be seen from the curves that the strength of US-680 is distinctly higher than that of non-US. Accurately, the YS and tensile strength of US-680 reach to 171 and 304 MPa, which are 23 and 19 MPa higher than that of non-US, respectively. Moreover, the plastic strain ratio (r) value of US-680

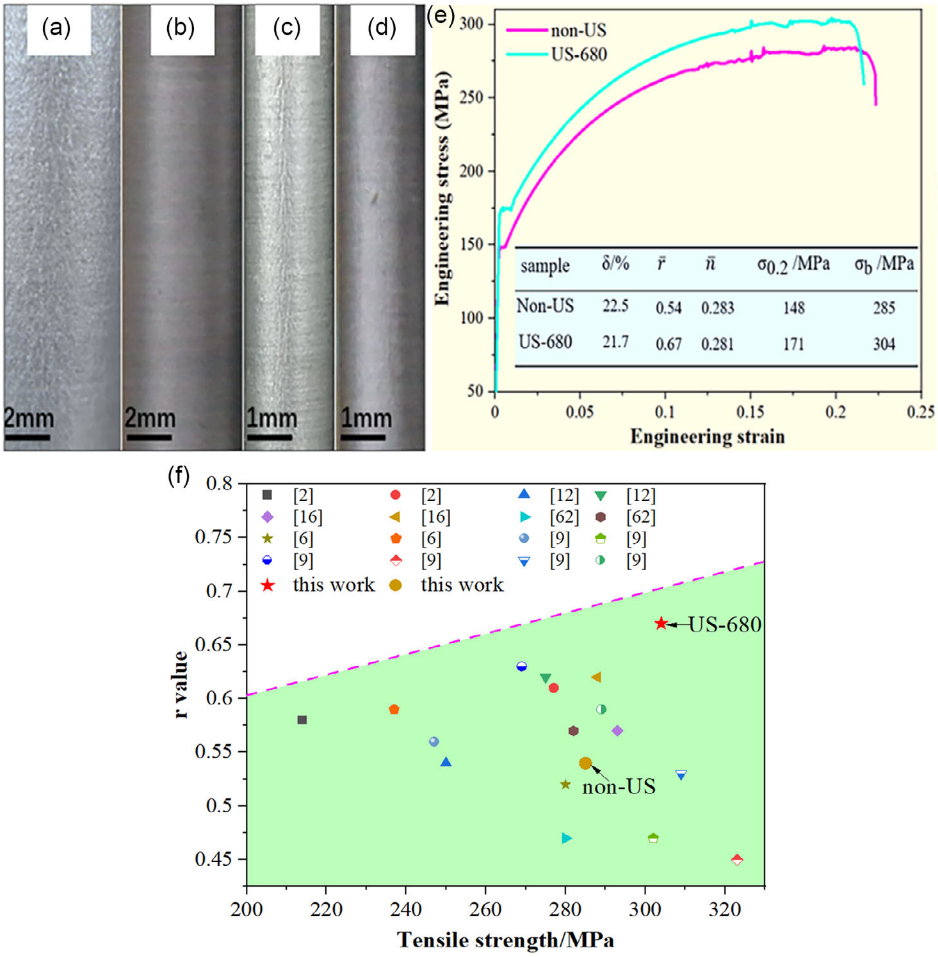

sample	δ/%	$\bar{r}$	$\bar{n}$	$\sigma_{0.2}$ /MPa	σ_b /MPa
Non-US	22.5	0.54	0.283	148	285
US-680	21.7	0.67	0.281	171	304

Figure 5. Bendability and mechanical properties of the non-US and US-680 pre-aged sheets. a) $R/t = 1$ of non-US; b) $R/t = 1$ of US-680; c) $R/t = 0.5$ of non-US; d) $R/t = 0.5$ of US-680; e) engineering stress–strain curves and tensile property parameters of non-US and US-680; and f) comparison of r value and tensile strength in kindred 6xxx pre-aged alloys sheets.

reaches to 0.67, which is 25% higher than that of non-US, meaning superior formability of US-680, consistent with the results of bending test. The *r* value and tensile strength of the two samples in this work are compared to kindred 6xxx alloys sheets in pre-aged condition, as shown in Figure 5f. The desirable quadrant of this plot is the upper right corner, that is, excellent combination of formability and strength. To the best of our knowledge, the US-680 pre-aged sheet has the best combination of formability and strength compared to other studies.

3.3. Recrystallization Microstructure and Texture

As is known to all, microstructure and texture of materials are the keys to the properties. Hence, it is necessary to further characterize the microstructure and texture of the pre-aged sheets non-US and US-680 due to their substantial property differences. Because the pre-aging treatment has no effect on the grain size, texture, and dispersion particles of the sheets, the pre-aged sheets can be substituted by solution treated sheets as the sample for characterization. **Figure 6** shows the recrystallization texture and corresponding grain size of solution-treated sheets non-US and US-680.

Obviously, it can be observed from Figure 6a,b that nearly equiaxed grains are dominant in both alloy sheets, indicating that the recrystallization occurred completely. However, their grain sizes are different, as shown the grain size statistics in Figure 6c,d. The average, minimum, and maximum grain sizes of non-US are 15.9, 9.9, and 45.2 μm, respectively; but that of US-680 are only 9.8, 5.9, and 27.6 μm. The finer recrystallization grain structure of US-680 sheet should be relevant to the stronger PSN effect and pinning effect induced by the higher number density of coarse and fine Fe-rich particles.

The intensity and volume fraction of recrystallization texture are summarized in **Table 3**. The Cube orientation and Cube$_{\mathrm{ND}}$ orientation are the main texture components in both the alloy sheets. In addition, the non-US sheet possesses additional P {011}<122> orientation and a small amount of Copper{112}<111> orientation and Brass{110}<112> orientation. Clearly, the intensity and volume fraction of each texture in sheet US-680 is smaller than that in sheet non-US, that is, sheet US-680 possesses weaker texture. Interestingly, US-680 has a higher volume fraction of Cube$_{\mathrm{ND}}$ orientation than non-US.

Finally, the dispersion particles in the α-Al matrix of solution-treated sheets non-US and US-680 were characterized by TEM. The bright-field TEM images showing the dispersoids viewed along the $[001]_{\mathrm{Al}}$ zone axis are shown in **Figure 7**a,b. It can be found that spherical nanoscale particles exist in both the sheets, but the particles in US-680 are smaller and much higher in number density. With the evidence of TEM energy dispersive X-ray

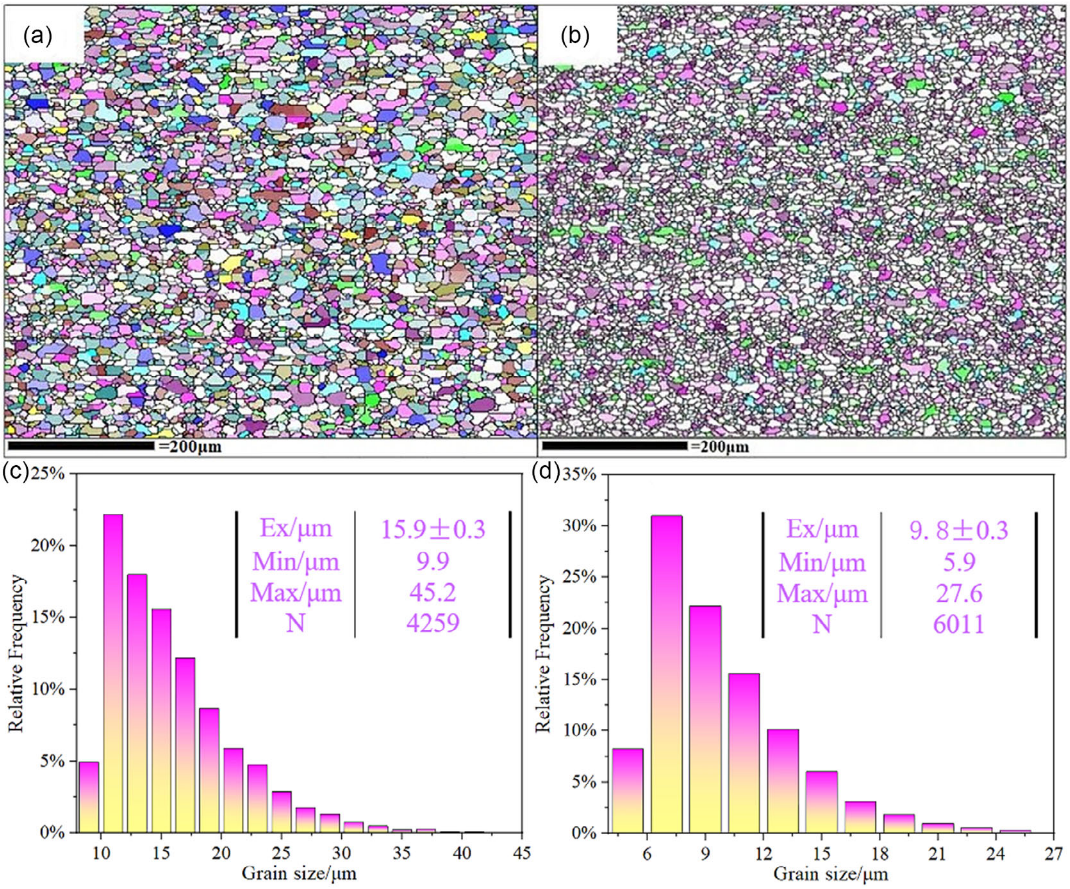

Figure 6. a,b) Recrystallization texture of non-US and US-680 in solid solution condition, respectively; c,d) recrystallization grain size statistics of non-US and US-680, respectively.

Table 3. Intensity and volume fraction of the textures in solution-treated alloy sheets.

Sample	Component	Cube	$Cube_{ND}$	Copper	Brass	$Cube_{RD}$	P
Non-US	Intensity	2.9	2.6	1.38	1.23	1.84	1.97
	VF/%	13.7	8.6	5.1	3.6	10.2	8.48
US-680	Intensity	1.8	2.1	–	–	1.1	–
	VF/%	6.8	16.4	–	–	5.3	–

spectroscopy and selected area electron diffraction patterns analysis on the particles, as shown in Figure 7c,d, it is proved that these particles are all Al(Fe,Mn)Si dispersoids.

4. Discussion

4.1. Effect of USMT on the Formation of Fe-Rich Phase

On the basis of thermal calculation simulation for the alloy studied in present work by *Thermo-Calc 2021a* software, the relationship between the amount of all phases and the solidification temperature are shown in **Figure 8**. It can be seen that the formation temperatures of FCC_Al and β-Fe-rich phase are about 650 and 632 °C, respectively, while the both are completed at the same temperature of about 595 °C, indicating that the formation of β-Fe-rich phase follows the crystallization of FCC_Al, and eutectic behavior between them exists. Hence, the morphology and distribution of β-Fe-rich phase are certainly related to the formation of as-cast grains and the solutes distribution in front of FCC_Al solidification interface.

To clearly reveal the effect of USMT on the formation β-Fe-rich phase, the schematic solidification diagrams of non-US and US-680 were proposed. **Figure 9**a–c presents the schematic solidification process of non-US. After smelting of raw materials, the melt is maintained at a constant temperature of 680 °C at which the melt is fully liquidus. Many studies have suggested that the most important characteristic of liquid metal microstructure is short-range order and long-range disorder of atomic structure.[45–47] Therefore, certainly, short-range ordered Al-atomic structure (which is more likely to develop into crystal nuclei with energy fluctuation) exists in the 680 °C melt, and solutes are evenly distributed within the bulk (Figure 9a). After the melt is poured into mold, nonequilibrium solidification immediately occurs due to powerful constitutional undercooling. At the initial stage, homogeneous and heterogenous nucleation occur simultaneously resulting in the formation of equiaxed and incipient dendritic FCC_Al crystal with solutes enriched at the

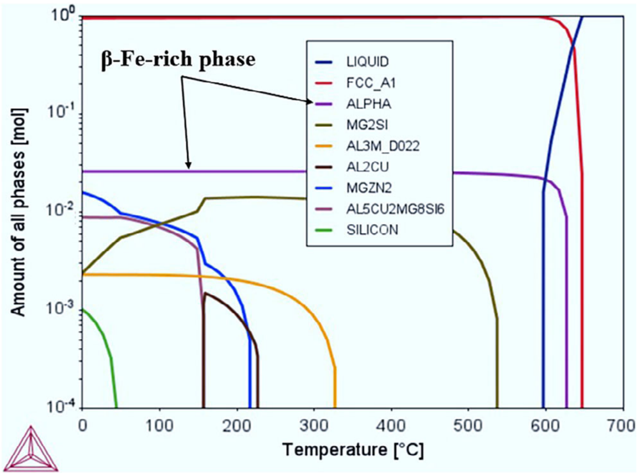

Figure 8. Relationship between the amount of all phases and the solidification temperature of the alloy studied in present work.

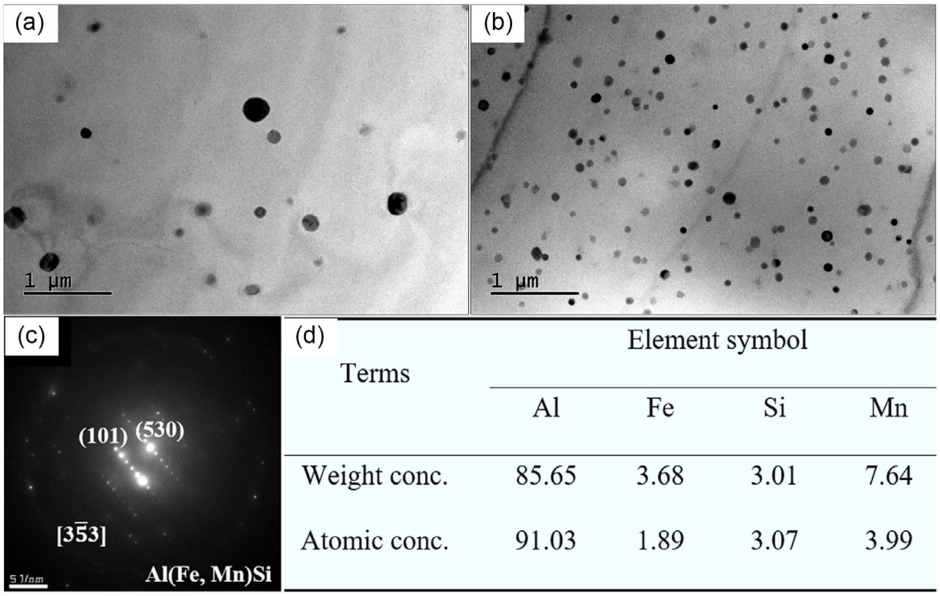

Terms	Element symbol			
	Al	Fe	Si	Mn
Weight conc.	85.65	3.68	3.01	7.64
Atomic conc.	91.03	1.89	3.07	3.99

Figure 7. Transmission electron microscope (TEM) characterization of dispersoids in pre-aged sheets non-US and US-680: a) dispersoids in non-US; b) dispersoids in US-680; c) selected area electron diffraction pattern of Al(Fe,Mn)Si particle; and e) chemical composition of Al(Fe,Mn)Si particle.

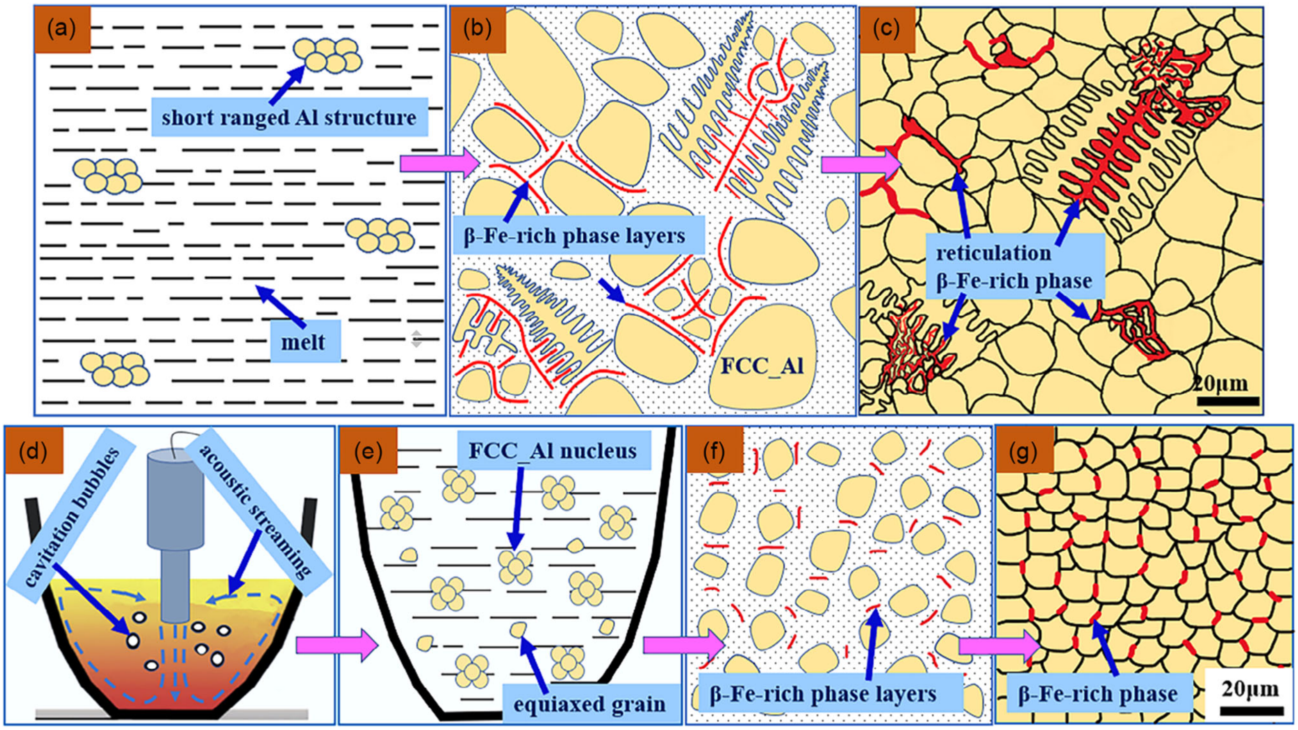

Figure 9. a–c) Schematic solidification diagrams of non-US; d–g) schematic solidification diagrams of US-680.

solid–liquid interface front, which lays the foundation for the microsegregation of β-Fe-rich phase. With the decrease of solidification temperature, Fe, Mn, and Si atoms continue to enrich at the front of solidification interface, and are bonded with Al atom, forming slender β-Fe-rich phase layers, just shown as Figure 9b. Whereafter, with the coarsening of dendrite arms as well as the growth of equiaxed grains, a point at which the dendrites and equiaxed grains become mechanically interlocked with each another is reached, and then a rigid network is established.[48] Once the enclosed zone forms, the β-Fe-rich phase layers and a certain volume of melt are trapped in it, and the liquid-feeding mechanism will be unavailable, that is, the solutes content in the enclosed zone will not change. With the development of solidification, the trapped primary β-Fe-rich phase layers continue to coarsen by absorbing Al, Fe, Mn, and Si atoms in the surrounding melt. Simultaneously, new equiaxed grains are formed on superior nucleation sites, and new β-Fe-rich phase forms and extends along grain boundaries in the enclosed zone, resulting in the morphology of coarse reticulation (Figure 9c).

Figure 9d–g suggests the schematic solidification process of US-680. When USMT is initiated in the liquid condition, it is assumed that the melt is completely under the effect of cavitation bubbles and acoustic streaming,[49] which can significantly promote heterogeneous nucleation and elimination of dendrites. Specifically, 1) the melt undercooling at the bubbles surface induced by the evaporation of liquid inside the bubbles facilitates nucleation on the bubbles; 2) the huge pressure pulse and high cumulative jet arising from the collapse of bubbles improve the melting point (i.e., increase of undercooling), resulting in an enhanced nucleation; 3) collapse of cavitation bubbles boosts heterogeneous nucleation by wetting the impurities;[50–52] 4) moreover, the propagative ultrasonic wave in the melt can produce finite amplitude attenuation, which makes the melt form a certain sound pressure gradient from the sonotrode, leading to the melt flows at high speed. As the sound pressure amplitude exceeds a certain value, a fluid jet (namely, acoustic streaming) can be generated in melt. The streaming directly leaves the surface of the sonotrode and forms a circulation in the whole melt (Figure 9d). When the dendrites formed on the mold wall experience strong acoustic streaming, it was broken by the solid–liquid interface and turns into fine equiaxed grain.[53] Hence, a large number of FCC_Al nuclei and some fine equiaxed grains exist in the melt after USMT (Figure 9e). Then, during subsequent solidification, abundant equiaxed grains are formed rapidly with tiny β-Fe-rich phase layers evenly distributed at the front solid–liquid interface in the whole volume (Figure 9f). Finally, as the solidification is completed, the as-cast microstructure with significantly refined grains and fine short-rodlike β-Fe-rich phase evenly distributed along grain boundaries is formed (Figure 9g).

Accordingly, there is no doubt, the size and morphology of β-Fe-rich phase directly depend on the size and morphology of the enclosed zone. The coarse equiaxed grains and dendrites in non-US distinctly tend to form large and complex random enclosed zone, which is responsible for the formation of coarse reticulation β-Fe-rich phase (as shown in Figure 2a). However, after USMT, the rapid growth of abundant fine equiaxed grains inhibits the formation of complex enclosed zones, compressing the β-Fe-rich phase layers to grain boundaries, and finally forming fine short-rodlike β-Fe-rich phase (as shown in Figure 2c).

In addition, both cavitation bubbles and acoustic streaming have vital impact on solute diffusion, especially the acoustic streaming which plays a key role in accelerating mass and heat transfer. The parameter α of solute diffusion is defined as[54]

$$\alpha = \frac{D_0 \exp(-Q/RT)\tau}{l^2} \tag{1}$$

where D_0 is diffusion constant, R is gas constant, Q is activation energy, T is absolute temperature, τ is local solidification time, and l is diffusion length. When USMT is applied, the local temperature of the melt is raised due to the cavitation effect. Concurrently, the acoustic streaming promotes atomic diffusion, reduces thickness of diffusion layer, and impels the transmission and diffusion of excessive solutes that existed in solute-rich band at solidification front. All of these effects contribute to an enlarged α value. In other words, USMT promotes the diffusion of solute elements into the grains during solidification, resulting in the reduction of Fe, Mn, and Si content in the final β-Fe-rich phase (see Figure 2e,f).

4.2. Effect of USMT on the Transformation of β-Fe-Rich Phase

The size and distribution of Fe-rich particles could exert an important influence on recrystallization grains, texture, and mechanical property of alloy sheets. While the transformation of β-Fe-rich phase to α-Fe-rich phase (hereafter, referred to $\beta \rightarrow \alpha$ for short) is vital to the spheroidization and refinement of Fe-rich particles. Hence, it is necessary to study the effect of USMT on the transformation of β-Fe-rich phase during homogenization.

Generally, the process of $\beta \rightarrow \alpha$ includes two steps: the melting of β phase border (columnar diffusion) and nucleation of α phase (spherical diffusion), whose rate is directly determined by the concentration field formed by Fe diffusion.[55] Under appropriate assumptions about the diffusion process: 1) the diffusion coefficient is regarded as a constant independent of concentration during the transition; 2) the development of β-Fe-rich phase dissolving interface and α-Fe-rich phase growth interface meets the Stefan rule; and 3) the kinetic process of $\beta \rightarrow \alpha$ is mainly controlled by Fe element whose diffusion rate is lowest and its concentration in the diffusion field does not change with time as a steady diffusion process. Then, the transformation ratio $f(\alpha)$ of $\beta \rightarrow \alpha$ can be expressed as[56]

$$(\alpha) = \frac{V(\alpha)}{V(\alpha) + V(\beta)} = \frac{\frac{4}{3}\pi R^3}{\frac{4}{3}\pi R^3 + \pi l^2 d} \tag{2}$$

where $V(\alpha)$ and $V(\beta)$ are the volume fractions of α-Fe-rich phase and β-Fe-rich phase, respectively; R is the radius of α-Fe-rich phase; l and d are radius and thickness of β-Fe-rich phase, respectively. Based on Equation (2), the quantitative relationship between f (α) and size of primary β-Fe-rich phase can be well predicted. Consistent with the study in ref. [57], when the value of $d > 0.5$ μm, the complete transformation of $\beta \rightarrow \alpha$ will be difficult under a specific homogenization temperature and time. Based on previous discussion, the transformation schematic diagrams of $\beta \rightarrow \alpha$ are put forward as shown in **Figure 10**a,b.

During homogenization, when the ends or somewhere (suitable for the nucleation of α-Fe-rich phase) of β-Fe-rich phase reach the appropriate concentration conditions due to the diffusion of Fe and Si into Al matrix, the α-Fe-rich phase nucleus begins to form and grow by absorbing surrounding Fe, Si, and Mn atoms. For the β-Fe-rich phase with $d < 0.5$ μm, the atoms in the center of it tend to diffuse out completely, inducing

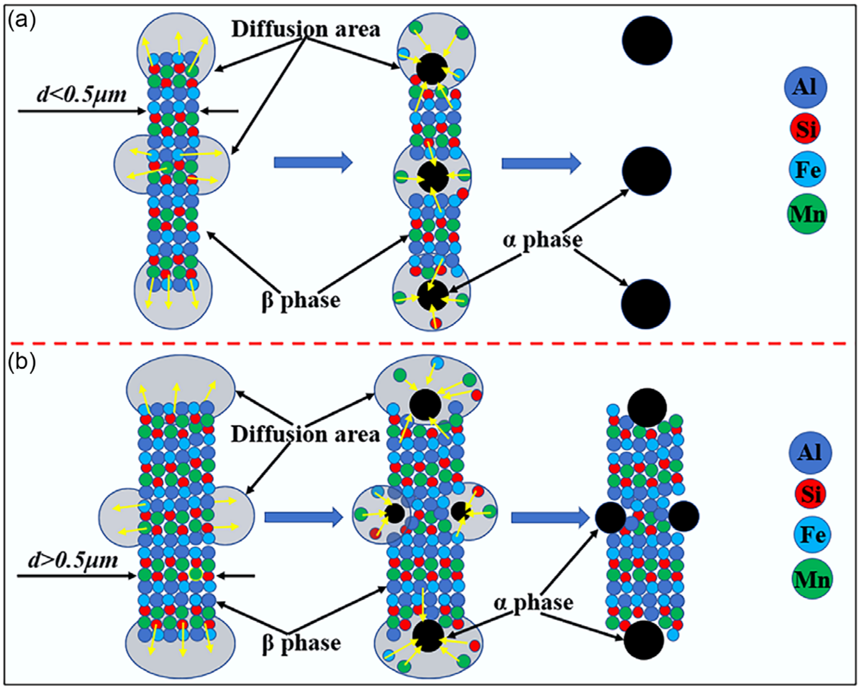

Figure 10. a,b) Transformation schematic diagrams of $\beta \rightarrow \alpha$: a) $d < 0.5$ μm and b) $d > 0.5$ μm.

complete fusing and spheroidization (Figure 10a). When $d > 0.5\ \mu m$, the central atoms of β-Fe-rich phase hardly diffuse under a specified homogenization temperature and time, resulting in that the nucleation of α-Fe-rich phase only occurs on surface and ends (Figure 10b). The d value of most coarse reticulation β-Fe-rich phase in as-cast non-US is much greater than 0.5, making it difficult to be transformed under the homogenization process in present work. And, only some slender β-Fe-rich phase branches with $d < 0.5$ are transformed to α-Fe-rich phase. That's why the number density of α-Fe-rich phase in homogenized non-US is quite low (see Figure 3a). Nevertheless, almost all of β-Fe-rich phase in as-cast US-680 have a d value less than 0.5, which is in favor of its transformation and leading to much higher number density of spherical α-Fe-rich phase (see Figure 3b).

4.3. Relationship between Fe-Rich Phase, Microstructure and Properties

As revealed in Section 3.2, the bendability and strength of the novel Al–Mg–Si–Cu–Zn–Fe–Mn alloy studied in present work are significantly improved by the coupling control of USMT and TMP. And, the effects of USMT on the formation of primary β-Fe-rich phase during solidification and transformation in homogenization have been reasonably discussed in Section 4.1 and 4.2. Here, the effect of Fe-rich particles on the grain refinement and texture weakening and the relationship between recrystallization microstructure and bendability as well as strength are further systematically revealed.

4.3.1. Effect of Fe-Rich Phase on Recrystallization Microstructure

As summarized by Huang,[44] the coarse particles (>1 μm) can provide enough recrystallization nucleation sites, and fine particles (>1 μm) can retard recrystallization grain growth by pinning the migration of grain boundary. In terms of increasing recrystallization nucleation sites, the more viable nuclei originating from the highly deformed zones around coarse Fe-rich particles may result in the development of a fine grain structure. Obviously, as shown in Figure 4c,d, the higher number density of coarse Fe-rich particles in sheet US-680 could lead to finer recrystallization grains. In contrast, from the aspect of retarding grain growth, the higher retarding force could also contribute to a fine grain structure. The Zener drag force Pz induced by the interaction of fine particles and boundaries is usually assumed to have the following expression[58]

$$P_Z = 3F_V\gamma_b/d_p \tag{3}$$

where F_V is the volume fraction of fine particles, γ_b is the grain-boundary energy with a value of $0.32\ J\ m^{-2}$ for aluminum alloys, and d_p is the average size of fine particles. Based on Equation (3) and the results in Table 2, it can be calculated that the F_V/d_p values in sheets non-US and US-680 are 0.05 and $0.13\ \mu m^{-1}$, respectively. Substituting the two values into Equation (3), the Zener drag force in sheets non-US and US-680 are calculated to be 0.48×10^5 and $1.25 \times 10^5\ J\ m^{-3}$, respectively. Clearly, sheet US-680 with USMT can exert a larger drag force. Therefore, sheet US-680 not only possesses more nuclei but also larger Zener drag force, which is responsible for the much finer recrystallization grains (see Figure 6a,b).

It is commonly believed that the nucleation site of Cube is related to cubic or transition bands, while the Cube_{ND} is related to deformation zones around the second-phase particles (>1 μm).[59] Moreover, the predominance of PSN in aluminum alloys during recrystallization could give rise to a weak texture. In other words, the higher number density of coarse Fe-rich particles in US-680 lead to its weaker texture. Considering the PSN nuclei relationship of $N_{\text{US-680}} > N_{\text{non-US}}$, the volume fraction relationship of Cube_{ND} should be $V_{\text{US-680}} > V_{\text{non-US}}$, which is consistent with the experimental result, as listed in Table 3. Additionally, it has been proposed that texture could be significantly influenced by grain size, and large grain size always tends to strengthen texture.[60] So, the finer grains of US-680 should be another reason for its weaker texture.

4.3.2. Mechanism of Improved Bendability and Strength in US-680

As is well known, excellent deep drawability is definitely conducive to bending molding. In other words, the factors improving deep drawability of alloy sheet can be considered to be favorable for better bendability. Generally, the limiting drawing ratio (LDR), which is closely related to the r and n values, is regarded as a relatively precise parameter to evaluate deep drawability, and can be expressed as follows[61]

$$\text{LDR} = \sqrt{\exp\left[(2f\exp(-n))\sqrt{\frac{1+\bar{r}}{2}}\right] + \exp\left[2n\sqrt{\frac{1+\bar{r}}{2}}\right] - 1} \tag{4}$$

where f is the factor of drawing efficiency and usually selected as 0.9. Substituting the $\bar{r}$ and n values in Figure 5e, the calculated LDR values of sheets non-US and US-680 are 2.01 and 2.06, respectively. Obviously, sheet US-680 possesses the better deep drawability (i.e., bendability), which is consistent with the bending test results in Figure 5a–d.

It is well accepted that the r value is mainly determined by the specific texture component and the corresponding volume fraction. Specifically, compared to Cube orientation, Cube_{ND} orientation is more beneficial to r value; Q and P orientations are both detrimental to r value;[62] moreover, weak texture always is in favor of enhanced r value. Accordingly, the improved bendability of sheet US-680 can be ascribed to the weaker texture, higher volume fraction of Cube_{ND} orientation and absence of P orientation.

The strength of Al–Mg–Si alloys is generally calculated as follows[63]

$$\sigma_y = \frac{k}{\sqrt{d}} + \sigma_0 + \sigma_{\text{dis}} + \sigma_{\text{ss}} + \sigma_{\text{ppt}} \tag{5}$$

where k is the strengthening coefficient with a value of $0.07\ \text{MPa}\ m^{1/2}$; d is the effective grain size; σ_0 is the intrinsic strength of pure Al (10 MPa), σ_{dis} represents the strength due to dislocation, σ_{ss} is the contribution caused by elements in solid solution, and σ_{ppt} is the strength contribution from dispersoids/precipitates. In present work, the YS of pre-aged sheet US-680 is 23 MPa larger than that of non-US, that is, $\Delta\sigma\gamma = \sigma\gamma_{us\text{-}680}–\sigma\gamma_{non\text{-}us} = 23$ MPa. Moreover, due to the non-US and US-680 share an exact same chemical composition, that is, $\sigma ss_{us\text{-}680} = \sigma\gamma_{non\text{-}us}$, so the contribution of σ_{ss} for the $\Delta\sigma\gamma$ can be ignored. Therefore, the increment of strength is mainly attributed to the difference of grain size, dislocation, and dispersoids/precipitates.

First, in terms of grain size, the strength from grain-boundary strengthening can be calculated by the Hall–Petch

$$\sigma = k/\sqrt{d} + \sigma_0 \tag{6}$$

Substituting the recrystallization grain size of non-US and US-680, 15.9 and 9.8 μm, respectively, the calculated $\sigma_{non\text{-}US}$ and $\sigma_{US\text{-}680}$ are 18 and 22 MPa. In other words, the contribution of fine grain strengthening to $\Delta\sigma\gamma$ is 4 MPa.

Second, from the aspect of dispersion/precipitates strengthening, since the β''/β' precipitates has not formed in the pre-aging condition, only dispersoid strengthening is considered for σ_{ppt}. In the absence of the β''/β' precipitates strengthening effect, the strength caused by dispersoids is predicted using the Orowan bypass equation expressed as follows[64]

$$\Delta\sigma_{or} = \frac{0.84MGb}{2\pi(1-\nu)^{1/2}\lambda}\ln\frac{r_d}{b} \tag{7}$$

where M is the Taylor factor, which is taken as $M = 3$; b is the Burger vector of Al (0.286 nm); G is the shear modulus (26.5 GPa); r_d is the equivalent radius of the dispersoids; ν is Poisson's ratio ($\nu = 0.3$); and λ is interparticle spacing ($\lambda = r_d\sqrt{2\pi/3f_d}$, where f_d is the volume fraction of the dispersoids, and can be calculated according to the Equation (1) in ref. [64]. The calculated values of related parameters on the basis of Figure 7a,b are listed in **Table 4**.

Substituting these values into Equation (7), the calculated strengths induced by dispersion strengthening of sheet non-US and US-680 are 24 and 39 MPa, meaning that the contribution of dispersion strengthening to $\Delta\sigma_y$ is 15 MPa. Clearly, the remaining 4 MPa strength increment is attributed to dislocation strengthening. In general, the fine grain strengthening, dispersion strengthening and dislocation strengthening are responsible for the improved strength of US-680, and dispersion strengthening resulted from finer and denser Al(FeMn)Si dispersoids is the dominant one.

5. Conclusions

In present work, the formation, evolution, and distribution of the primary Fe-rich phases in Al–Mg–Si–Cu–Zn–Fe–Mn alloy were coupling controlled by the USMT and TMP, so as to regulate microstructure and texture of the alloy sheets. Finally, the bendability and mechanical property of the pre-aged sheets are investigated. The following main conclusions can be drawn: 1) For the Al–Mg–Si–Cu–Zn–Fe–Mn alloy studied in present work, the optimum temperature for implementation of USMT is 680 °C. USMT at 680 °C can reduce the as-cast grain size from 30 to 15 μm, and concurrently, change the primary β-Fe-rich phase from coarse reticulation to fine short rod (with thickness < 0.5 μm) and decrease the Fe, Mn, and Si content in it. The transformation of β-Fe-rich phase to α-Fe-rich phase during homogenization concerns diffusion of Fe and Si elements, and absorption of Mn. 2) Coupling control of USMT and TMP can decrease the average size, increase the number density, and improve the distribution uniformity of both coarse and fine Fe-rich particles, resulting in a fine-grained recrystallization microstructure and weakened texture, which is responsible for the best combination of formability and strength of the pre-aged sheet. 3) USMT refines the Al(FeMn)Si dispersoids formed during homogenization and significantly increases its number density, which makes dispersion strengthening a dominant contributor to the improved strength.

Table 4. The r_d, f_d, and λ of Al(FeMn)Si dispersoid in solution-treated non-US and US-680.

Alloy	r_d [nm]	f_d [%]	λ [nm]
Non-US	50	0.86	780
US-680	42	1.6	469

Acknowledgements

This work was supported by the National Key Research and Development Program of China (Grant no. 2021YFE0115900), National Natural Science Foundation of China (Grant nos. 51871029, 51571023, and 51301016), Government-Guided Program Intergovernmental Bilateral Innovation Cooperation Project (Grant no. BZ2019019), the Opening Project of State Key Lab of Advanced Metals and Materials (Grant nos. 2020-ZD02 and 2022-Z03), and Industry–University Cooperation Collaborative Education Project (Grant nos. 202102437001 and 202102437002).

Conflict of Interest

The authors declare no conflict of interest.

Data Availability Statement

The data that support the findings of this study are available on request from the corresponding author. The data are not publicly available due to privacy or ethical restrictions.

Keywords

Al–Mg–Si–Cu–Zn alloy, bendability, Fe-rich phase, strength, ultrasonic melt treatment

Received: March 16, 2023
Revised: May 14, 2023
Published online:

---

[1] M. Werinos, H. Antrekowitsch, T. Ebner, *Acta Mater.* **2016**, *118*, 296.
[2] L. Zhu, M. X. Guo, J. S. Zhang, *Mater. Sci. Eng. A* **2021**, *826*, 142013.
[3] G. H. Tao, C. H. Liu, J. H. Chen, P. P. Ma, L. M. Liu, *Mater. Sci. Eng. A* **2015**, *642*, 241.

[4] J. H. Kim, C. D. Marioara, R. Holmestad, E. Kobayashi, T. Sato, *Mater. Sci. Eng. A* **2013**, *560*, 154.

[5] X. K. Yang, B. Q. Xiong, X. W. Li, L. Z. Yan, *J. Cent. South Univ.* **2021**, *28*, 2636.

[6] X. F. Wang, M. X. Guo, A. Chapuis, J. R. Luo, J. S. Zhang, L. Z. Zhuang, *Mater. Sci. Eng. A* **2015**, *17*, 137.

[7] S. Zhu, Z. H. Li, L. Z. Yan, S. H. Huang, H. W. Yan, Y. A. Zhang, *Mater. Charact.* **2018**, *145*, 258.

[8] M. X. Guo, G. Sha, L. Y. Cao, W. Q. Liu, J. S. Zhang, L. Z. Zhuang, *Mater. Chem. Phys.* **2015**, *162*, 15.

[9] X. F. Wang, M. X. Guo, J. S. Zhang, L. Z. Zhuang, *Mater. Sci. Eng. A* **2016**, *677*, 522.

[10] J. Sidor, A. Miroux, R. Petrov, L. Kestens, *Acta Mater.* **2008**, *56*, 2495.

[11] M. H. Khan, A. Das, Z. Li, H. R. Kotadia, *Intermetallics* **2021**, *132*, 107132.

[12] M. X. Guo, J. Zhu, Y. Zhang, G. J. Li, T. Lin, *Mater. Charact.* **2017**, *312*, 248.

[13] P. Castany, F. Diologent, A. Rossoll, J. F. Despois, A. Mortensen, *Mater. Sci. Eng. A* **2013**, *559*, 558.

[14] X. Liu, H. L. Jia, C. Wang, X. Wu, M. Zha, H. Y. Wang, *Mater. Sci. Eng. A* **2022**, *831*, 142256.

[15] X. F. Wang, M. X. Guo, J. R. Luo, J. Zhu, J. S. Zhang, L. Z. Zhuang, *Mater. Charact.* **2017**, *134*, 123.

[16] X. F. Wang, M. X. Guo, L. Y. Cao, J. R. Luo, J. S. Zhang, L. Z. Zhuang, *Mater. Sci. Eng. A* **2015**, *621*, 8.

[17] S. G. Shabestari, *Mater. Sci. Eng. A* **2004**, *383*, 289.

[18] L. S. Weet, S. X. Gao, S. Zhu, J. A. Taylor, *Metall. Mater. Trans. A* **2011**, *42*, 1737.

[19] J. S. Wang, P. D. Lee, R. W. Hamilton, M. Li, J. Allison, *Scr. Mater.* **2009**, *60*, 516.

[20] Y. L. Zhao, W. W. Zhang, D. F. Song, *J. Mater. Sci. Technol.* **2021**, *80*, 84.

[21] C. Lin, S. S. Wu, G. Zhong, L. Wan, P. An, *Trans. Nonferrous Met. Soc. China* **2013**, *23*, 1245.

[22] M. Y. Cao, H. Hu, X. D. Jia, S. J. Tian, C. C. Zhao, X. B. Han, *J. Manuf. Process.* **2020**, *59*, 690.

[23] H. R. Kotadia, M. Qian, A. Das, *J. Alloys Compd.* **2020**, *823*, 153833.

[24] J. W. Cao, S. Shuai, C. L. Huang, T. Hu, C. Y. Chen, J. Wang, Z. M. Ren, *Intermetallics* **2022**, *143*, 107471.

[25] T. Radetić, M. Popović, A. Alil, B. Markoli, I. Naglič, E. Romhanji, *J. Alloys Compd.* **2022**, *902*, 163719.

[26] N. Bayat, T. Carlberg, M. Cieslar, *J. Phys. Chem. Solids* **2019**, *130*, 165.

[27] A. Wagiman, M. S. Mustapa, R. Asmawi, S. Shamsudin, *Int. J. Adv. Manuf. Technol.* **2020**, *106*, 641.

[28] D. G. Eskin, I. Tzanakis, F. Wang, G. S. B. Lebon, T. Subroto, K. Pericleous, J. Mi, *Ultrason. Sonochem.* **2019**, *52*, 455.

[29] F. Wang, D. Eskin, J. W. Mi, C. N. Wang, B. Koe, A. King, C. Reinhard, T. Connolley, *Acta Mater.* **2017**, *141*, 142.

[30] Z. G. Zhang, C. N. Wang, B. Koe, C. M. Schlepütz, S. Irvine, J. W. Mi, *Acta Mater.* **2021**, *209*, 116796.

[31] B. Wang, D. Y. Tan, T. L. Lee, *Acta Mater.* **2018**, *144*, 505.

[32] H. S. Jang, G. H. Lee, J. B. Jeon, Y. S. Choi, S. Shin, *J. Mater. Res. Technol.* **2022**, *19*, 2645.

[33] X. T. Li, T. J. Li, X. M. Li, J. Z. Jin, *Ultrason. Sonochem.* **2006**, *13*, 121.

[34] X. R. Chen, F. K. Ning, J. Hou, Q. C. Le, Y. Tang, *Ultrason. Sonochem.* **2018**, *40*, 433.

[35] C. Lin, Ph.D. Thesis, *Huazhong University of Science & Technology*, **2014**.

[36] M. Sha, S. S. Wu, L. Wan, *Mater. Sci. Eng. A* **2012**, *554*, 142.

[37] A. Thirugnanasambandama, T. Selvakumaran, R. Subbiah, K. Ramachandran, S. Manickam, *Ultrason. Sonochem.* **2021**, *76*, 105631.

[38] F. Wang, I. Tzanakisb, D. Eskinc, J. W. Mi, T. Connolley, *Ultrason. Sonochem.* **2017**, *39*, 66.

[39] M. F. Qi, Y. Z. Xu, J. Y. Li, Y. L. Kang, Z. Wulabieke, *Corros. Sci.* **2021**, *180*, 109180.

[40] C. J. Todaro, M. A. Easton, D. Qiu, G. Wang, D. H. StJohn, M. Qian, *Metall. Mater. Trans. A* **2017**, *48*, 5579.

[41] C. J. Todaro, M. A. Easton, D. Qiu, G. Wang, D. H. StJohn, M. Qian, *J. Mater. Process. Technol.* **2019**, *271*, 346.

[42] Z. T. Liu, B. Y. Wang, C. Wang, *J. Mater. Sci. Technol.* **2020**, *41*, 178.

[43] B. Yuan, G. J. Li, M. X. Guo, L. Z. Zhuang, *J. Mater. Res. Technol.* **2021**, *15*, 5059.

[44] K. Huang, K. Marthinsen, Q. L. Zhao, R. E. Logé, *Prog. Mater. Sci.* **2018**, *92*, 284.

[45] J. Teixeira, *Mater. Sci. Eng. A* **1994**, *178*, 9.

[46] Q. H. Zheng, T. Hu, S. L. Roux, *J. Rare Earths* **2022**.

[47] X. F. Bian, M. H. Sun, X. Y. Xue, X. B. Qin, *Mater. Lett.* **2003**, *57*, 2001.

[48] I. Steinbach, H. J. Diepers, C. Beckermann, *J. Cryst. Growth* **2005**, *275*, 624.

[49] G. Wang, P. Croaker, M. Dargusch, D. McGuckin, D. StJohn, *Comput. Mater. Sci.* **2017**, *134*, 116.

[50] C. E. H. Tonrya, G. Djambazova, A. Dybalskab, W. D. Griffiths, C. Beckwith, V. Bojarevics, K. A. Pericleous, *Ultrason. Sonochem.* **2020**, *63*, 104959.

[51] M. Qian, A. Ramirez, A. Das, *J. Cryst. Growth* **2009**, *311*, 3708.

[52] J. Y. Li, S. L. Lü, S. S. Wu, Q. Gao, *Ultrason. Sonochem.* **2018**, *42*, 814.

[53] N. Balasubramani, G. Wang, D. H. Stjohn, M. S. Dargusch, *J. Mater. Sci. Technol.* **2021**, *65*, 38.

[54] M. M. Duan, C. L. Chen, *Acta Metall. Sin.* **2010**, *46*, 885.

[55] L. Y. Cao, M. X. Guo, H. Cui, Y. H. Cai, Q. X. Zhang, X. Q. Hu, J. S. Zhang, *Acta Metall. Sin.* **2013**, *49*, 428.

[56] N. C. W. Kuijpers, F. J. Vermolen, C. Vuik, P. T. G. Koenis, K. E. Nilsen, *Mater Sci Eng A* **2005**, *394*, 9.

[57] N. C. W. Kuijpers, F. J. Vermolen, K. Vuik, *Mater. Trans.* **2005**, *44*, 1448.

[58] F. J. Humphreys, M. Hatherly, *Recrystallization and Related Annealing Phenomena, seconded*, Elsevier, Oxford **2004**.

[59] K. Lücke, O. Engler, *Mater. Sci. Technol.* **1990**, *6*, 1113.

[60] A. Morawiec, *Scr. Mater.* **2011**, *64*, 466.

[61] X. F. Wang, M. X. Guo, A. Chapuis, J. R. Luo, J. S. Zhang, L. Z. Zhuang, *Mater. Sci. Eng. A* **2015**, *633*, 49.

[62] J. Sidor, A. Miroux, R. Petrov, L. Kestens, *Philos. Mag.* **2008**, *88*, 3779.

[63] L. Zhu, M. X. Guo, J. S. Zhang, *Mater. Sci. Eng. A* **2022**, *841*, 143016.

[64] J. Rakhmonov, K. Liu, P. Rometsch, N. Parson, X. G. Chen, *J. Alloy. Compd.* **2021**, *861*, 157937.